1-1-2012

Volume of Fluid Simulations for Droplet Impact on Dry and Wetted Hydrophobic and Superhydrophobic Surfaces

Emily Nicole Burtnett

Volume of fluid simulations for droplet impact on dry and wetted hydrophobic and superhydrophobic surfaces

By

Emily Nicole Burtnett

A Thesis
Submitted to the Faculty of
Mississippi State University
in Partial Fulfillment of the Requirements
for the Degree of Master of Science
in Aerospace Engineering
in the Department of Aerospace engineering

Mississippi State, Mississippi

August 2012

Volume of fluid simulations for droplet impact on dry and wetted hydrophobic and superhydrophobic surfaces

By

Emily Nicole Burtnett

Approved:

David S. Thompson Associate Professor of Aerospace Engineering (Major Professor)	David H. Bridges Associate Professor of Aerospace Engineering (Committee Member)
Thomas E. Hannigan, III Instructor of Aerospace Engineering (Committee Member)	J. Mark Janus Associate Professor and Graduate Coordinator of Aerospace Engineering (Committee Member)
Sarah A. Rajala Dean of the James Worth Bagley College of Engineering	

Name: Emily Nicole Burtnett

Date of Degree: August 11, 2012

Institution: Mississippi State University

Major Field: Aerospace Engineering

Major Professor: David S. Thompson

Title of Study: Volume of fluid simulations for droplet impact on dry and wetted hydrophobic and superhydrophobic surfaces

Pages in Study: 51

Candidate for Degree of Master of Science

An aircraft may experience in-flight ice accretion and corresponding reductions in performance and control when the vehicle encounters clouds of super-cooled water droplets. The EADS-IW Surface Engineering Group is investigating passive anti-icing possibilities, such as functional and ice phobic coatings. Ice-resistant coatings require investigating droplet impact on dry surfaces and wet films, including microscopic effects such as droplet splashing. To investigate droplet impacts, a volume of fluid (VOF) flow solver was used for droplets impacting dry and wetted hydrophobic and superhydrophobic surfaces, focusing on meso-scale simulations. The effects of structured, micro-scale surface roughness and the effects of a thin wet film on the surface, corresponding to a saturated surface under high humidity conditions, were investigated. Axisymmetric domains produced acceptable results for smooth, dry surfaces. It was determined that in order to properly predict behavior of droplets impacting surfaces with structured micro-scale roughness, three-dimensional simulations are recommended.

DEDICATION

I would like to dedicate this thesis to my entire family, especially Alex and Dad and Mom. There is no doubt in my mind that without their continued support and counsel I could not have completed this process.

ACKNOWLEDGEMENTS

It is a pleasure to thank those who made this thesis possible. The support provided by EADS-North America and the contract monitor, Dr. Mark Fraser, which allowed me the opportunity to work on this project, are gratefully acknowledged. Support for this project was also provided by the National Science Foundation GK 12 program, under award # DGE-0947419 at Mississippi State University. Schools participating include the Columbus School District, Mississippi School for Math & Science, and the Starkville School District. I extend my gratitude to Dr. Dominik Raps and Mr. Stefan Jung at EADS-Innovation Works, for without their support and vision, this project would not have been possible. It is an honor for me to thank Dr. David Thompson for all his patience, inspirational instruction, and guidance. His kind but rigorous oversight of this thesis gave me the motivation to perform to the best of my ability. I was very fortunate to have been able to work with him on my Master's degree. I would also like to thank my committee members, Dr. David Bridges, Mr. Thomas Hannigan, and Dr. J. Mark Janus, for their time and expertise to better my work. I thank them for their contributions and good-natured support. I thank Ms. Sarah Radencic, Dr. Karen McNeil, and Dr. Donna Pierce for the opportunity to share my research with high school math students as a NSF INSPIRE GK-12 Fellow. I was extraordinarily fortunate to be a part of this program as it allowed me to enrich my research overseas at the University of Surrey, take high school students beyond their textbooks, and taught me to communicate my research in new ways. I would also like to thank Joey Jones and Dr.

Greg Burgreen of the MSU HPC and MSU CAVS, respectively, for their assistance installing and modifying OpenFOAM®.

I owe my deepest gratitude to Dad and Mom for instilling the importance of hard work and higher education. I am eternally indebted to them for their financial and emotional support along the way, and for moving my vast collections of "stuff" halfway across the United States twice. Words fail me to express my appreciation to Alex, whose dedication, love, and persistent confidence in me, has pulled me through the most difficult of days. How he manages to put up with me, I may never know, but I am forever appreciative. I would also like to thank his family for so graciously accepting me as a member of their family and for their thoughtful encouragement throughout my academic endeavors. I am grateful for God's provision of joys, challenges, and grace for growth.

Finally, I would like to thank everybody who was important to the successful culmination of this thesis process, and express my apology that I could not mention each of you personally.

TABLE OF CONTENTS

LIST OF TABLES

LIST OF FIGURES

LIST OF SYMBOLS

α_p, α_s	=	volume fraction of the primary and secondary phases
$\theta, \theta_0, \theta_A, \theta_R$	=	contact angle, static/advancing/receding contact angle
μ	=	viscosity, $N\text{-}s\text{-}m^{-2}$
ρ	=	density, $kg\text{-}m^{-3}$
σ	=	surface tension, $N\text{-}m^{-1}$
d	=	droplet diameter
f_b	=	body force per unit mass, $N\text{-}kg^{-1}$
H^*	=	dimensionless film thickness
h_0	=	film thickness
n_{wall}	=	normal to the wall
p	=	pressure, $N\text{-}m^{-2}$
t_{wall}	=	tangent to the wall
T	=	deviatoric viscous stress tensor, $N\text{-}m^{-2}$
u_θ	=	velocity scaling parameter for dynamic contact angle, $m\text{-}s^{-1}$
u_{wall}	=	velocity parallel the wall, $m\text{-}s^{-1}$
V, V_r, V_o	=	fluid velocity, relative fluid velocity, droplet impact velocity
CA	=	contact angle
CPR	=	cells per radius
DCA	=	dynamic contact angle

MRE	=	micro-scale roughness element
SCA	=	static contact angle
SLD	=	super-cooled large droplet
VOF	=	volume of fluid method
Oh	=	Ohnesorge number
Re	=	Reynolds number
We	=	Weber number

CHAPTER I

INTRODUCTION

1.1 Background

Ice accretion and adhesion on surfaces are issues of concern in the aviation field. Even ice accretion that is barely visible on aerodynamic surfaces, which can cause a reduction in performance and control or on airflow measurement instruments may result in conditions detrimental to flight safety. In-flight ice accretion occurs when an aircraft encounters a cloud of super-cooled water droplets which impinge on the surfaces of the aircraft and freeze. The Federal Aviation Administration (FAA) CFR (Code of Federal Regulations) Title 14 Part 25 Appendix C [54] discusses ice protection for aircraft during flight. An aircraft must demonstrate the capability to operate safely in continuous maximum and intermittent maximum icing conditions to be certified for flight in icing conditions, as specified in Appendix C. To gain this certification, there are three types of deicing systems commonly employed on aircraft [27]: pneumatic, electromechanical-expulsion, and thermal deicing systems. A pneumatic deicing boot is a rubber bladder that is secured to the leading edge of an airfoil. When the boot is inflated, the accreted ice is cracked and detaches from the surface. An electro-mechanical system uses mechanical vibrations to break ice off vital surfaces. A weeping wing emits a chemical coating, covering the vital surfaces to prevent ice accretion. Thermal systems employ a series of flexible coils or bleed air from the engine to apply heat to critical surfaces which, in return, prevents any accreted ice.

Tragic accidents such as American Eagle Flight 4184 [55] in October 1994 near Roselawn, IN and Comair Flight 3272 [56] in January 1997 near Monroe, MI resulted in widespread research into aircraft icing avoidance and prevention. This research primarily focused on super-cooled large droplet (SLD) icing conditions that were the probable cause of both accidents. Both aircraft were equipped with pneumatic deicing boots; however, SLD ice and warm ambient temperatures caused significant liquid water run back resulting in a ridge of ice accretion on unprotected surfaces of the wing beyond the deicing boot. More recently, preliminary findings from the investigation into the crash of Air France Flight 447 have attributed inaccurate airspeed readings, which contributed to the crash, to ice buildup in the pitot tubes [8].

The circumstances of the American Eagle Flight 4184 incident show that ice may accrete rapidly and further demonstrate that ice formation on unprotected surfaces can create an unrecoverable situation. This example also illustrates that a pneumatic boot may provide insufficient protection for some icing situations. Additionally, thermal methods consume large amounts of energy and selective heating for melting ice relies on imperfect detection and activation techniques that may introduce serious risks. It is evident that current anti-icing methods are plagued by complications and there is an obvious demand for effective passive systems, or possibly hybrid systems, which would protect all aerodynamic surfaces, significantly reducing the potential of ice accumulation during flight.

In the context of "green" aircraft, such as a predominantly electric aircraft, bleed-less deicing systems have become the trend [10]. Because future electrical de-icing systems, such as the previously mentioned electro-thermal or electro-mechanical, as well as hybrid systems, will inevitably require reduced energy consumption, support of these

systems by passive approaches will be valuable for overall de-icing performance. Unique to existing approaches, passive systems seek to prevent or reduce ice accretion rather than attempting to remove ice after formation has occurred.

The European Aeronautic Defense and Space Company-Innovation Works (EADS-IW) Surface Engineering group is investigating passive anti-icing possibilities, such as functional and ice phobic coatings. Ice-resistant coatings require investigating droplet impact on dry surfaces and wet films, including microscopic effects such as droplet splashing or water crystallization. Such phenomena are closely related to the surface properties of wetting behavior, chemical functionality, and roughness. According to de Gennes [17], the wetting of the surface is "connected to physical chemistry (wettability), to statistical physics (pinning of the contact line, wetting transitions, etc.), to long-range forces (van der Waals, double layers), and to fluid dynamics." The subject is further complicated by the fact that the impact of a water droplet on an aerodynamic surface is a multi-scale problem. At large scales, the droplet trajectory is determined by the flow field in the vicinity of the aircraft. At molecular scales, the interface between the droplet and the surface is defined by the chemical composition of each.

There is a need for inexpensive and rapid testing of the icing-related properties of various ice-phobic surfaces, as there are many parameters to be prescribed for suitable coating development. Superhydrophobicity is typically accomplished using a combination of nano-scale surface roughness and chemical properties of the surface [40]. Additionally, structured, micro-scale roughness elements also offer promise for enhancing the surface's resistance to water collection, which is a necessary precursor to ice growth [34], [59]. Numerical simulation using computational fluid dynamics (CFD) is a prospect for such testing; but the complex physics and contrasting length scales

ranging over multiple orders of magnitude present considerable challenges for simulations.

1.2 Primary Contributions

The primary contribution of this research is the evaluation of the performance of structured micro-scale roughness elements (MREs) [34], [59] under high humidity conditions. Previous research has shown that significant performance degradation in hydrophobicity occurs after a nano-composite coating undergoes prolonged exposure to water vapor and 25 micron water droplets [16]. Specifically, the focus here is on the spread and rebound of droplets on smooth surfaces and surfaces with the MRE under dry and wet-film conditions.

A secondary contribution of this research is the validation of an open-source Volume of Fluid (VOF) solver for droplets on dry hydrophobic and superhydrophobic surfaces [17]. The fluid dynamics problem of interest is the incompressible, laminar flow of two, immiscible fluids, both of which are assumed to be Newtonian. The solution of the governing equations, a pressure-based formulation of the Navier-Stokes equation, is accomplished in OpenFOAM® 2.0 via the VOF approach [38]. Although its origins date back to the 1980s, OpenFOAM® is an open-source, comparative newcomer to the CFD community. The results reported here focus on meso-scale, i.e., droplet-scale, simulations. This requires modeling to describe the sub-droplet-scale physics, and the approach employed here utilizes a wall adhesion model modified to account for a specified contact angle [47].

1.3 Outline of Thesis

A literature review was performed to examine several important aspects of the present research. A survey of the occurrences and applications of superhydrophobic surfaces was performed to provide an understanding of recent advances in surface engineering leading to superhydrophobicity, including a review of their functions and applications to date and the design of current ice resistant coatings. For the numerical simulation of two immiscible fluids, multiphase flow capabilities in existing CFD software packages were investigated and examined for accuracy. Similar studies of water droplets impacting a dry surface, which utilize both experimental data and numerical calculations, provided guidance for this work. A brief overview of the computational methods used, the CFD package, and the mesh generation covers the fundamentals for the numerical fluid dynamics calculations.

The results of the present work are then discussed. In this section, the problem description including the mesh generation process and the boundary conditions of the numerical simulations are defined. The final sections of results elaborate on cases used for code validation and the cases of interest in this work including the effects of surface roughness, and the effect of a thin wet film, representing a saturated surface under conditions of high humidity.

CHAPTER II

LITERATURE REVIEW

The wettability of a surface is the ability of a liquid to maintain contact with a solid surface, therefore wetting it. Hydrophobicity is the physical property that causes a surface to repel water. Various degrees of wetting can be categorized by the contact angle, θ, which is defined as the angle between the wall and the tangent to the interface at the wall, measured inside the drop, as shown in Figure 2.1. Wettable surfaces are classified as hydrophilic, hydrophobic, or superhydrophobic surfaces based on contact angle, as shown in Figure 2.2. Characterized by a higher contact angle, a superhydrophobic surface demonstrates less wetting, and with a lower contact angle, a hydrophilic surface shows more wetting. This work is focuses on hydrophobic and superhydrophobic surfaces.

Figure 2.1 Schematic of contact angle

$\theta < 90°$	$90° < \theta < 150°$	$\theta > 150°$
Hydrophilic	Hydrophobic	Superhydrophobic

Figure 2.2 Categorization of fluid/surface wettability using the contact angle. Images taken by author using a Proscope®

2.1 Superhydrophobic Surfaces

One approach to ice prevention is stimulated by the biotechnology used by many organisms to control water droplets on their surfaces. Nature has produced surfaces that repel water using not only chemical properties but also geometrical properties. Recent biomimetic-based research by Gao *et al.* [22] has revealed that the compound on the eyes of mosquitoes possesses ideal superhydrophobic properties that allow them to maintain clear vision in a humid habitat. Autumn *et al.* [2] found that the superhydrophobic surface with nearly five hundred thousand keratinous microscopic hairs, or setae, on the surface of a gecko's foot allows it to climb rapidly up smooth vertical surfaces.

Similarly, Gao *et al.* [21] attribute the remarkable non-wetting legs of water striders—which allow them to stand with ease and move quickly on water—to the special hierarchical structure of their legs. The water strider's legs remain dry because they are covered in a large number of slanting tiny hairs with fine nano-grooves. Zheng *et al.* [61] showed that directional adhesion properties on the superhydrophobic wings of the butterfly are a result of a direction-dependent arrangement of flexible nano-tips on ridging nano-strips and micro-scales overlapped on the wings. This property of the wing is of utmost importance to the stability of flight, providing the wings the ability to clean easily in watery environments and avoid dirt particle accumulation.

Numerous natural materials have inspired scientific advances in superhydrophobic surfaces. Several artificial superhydrophobic surfaces have been fabricated based on the lotus leaf [26]. The lotus leaf has a surface that allows it to remain clean despite its surroundings. It typically grows in swamps and shallow waters, but can emerge from muddy waters completely clean. The surface has roughness which prevents water droplets from spreading and causes them to form beads instead. This phenomenon is often referred to as the "lotus-effect," and has proven to be of great biological and technological significance [3]. Patankar [40] mimicked the micro-structure that produces the lotus effect and improved the water repelling ability of a surface by doubling the roughness structures and number of slender pillars.

The common theme among these naturally occurring instances of water repelling surfaces is a superhydrophobic surface that repels water not only chemically, but also geometrically with an assortment of bristles. The connection between surface roughness and wettability or particle deposition is well known [34]. Surface roughness increases the apparent contact angle, thereby amplifying hydrophobicity.

2.2 Design of Ice Resistant Coatings

Numerous efforts have focused on the advance of superhydrophobic surfaces for icephobicity. Cao *et al.* [11] developed a nonoparticle-polymer composite which demonstrates the anti-icing capabilities of superhydrophobic surfaces. Similarly, Mishchenko *et al.* [34] found from an experimental analysis of temperature-dependent droplet/surface interactions, that a highly-ordered superhydrophobic surface can be designed to remain ice-free at temperatures of -25 to -30 °C. This behavior was attributed to the designed surfaces' ability to repel water droplets prior to ice nucleation

by reducing the surface area and contact time of impinging water droplets. In other words, the droplets bounce off the surface before nucleation can occur, leaving the surface ice-free. Jung *et al.* [31] considered delaying water freezing on untreated and coated surfaces ranging from hydrophilic to superhydrophobic and used the delays to estimate icephobicity. They discovered unexpected longer freezing delays for surfaces with nanometer-scale roughness (smooth) and higher wettability (hydrophilic), concluding that the selection of the suitable icephobic surface for a specific technological application requires a comprehensive evaluation of freezing delay and liquid-shedding ability and their competing effects.

Among the most advanced simulation-based approaches, Xiao *et al.* [59] used a multi-scale simulation framework to predict the anti-icing performance of a variety of nano-composite coatings under in-flight conditions. Their framework accounts for the effects of surface chemistry as well as nano-scale and micro-scale roughness. It couples molecular dynamics simulations, which define the material properties and the effects of nano-scale roughness, with CFD simulations, including micro-scale roughness, to determine whether a droplet departs the surface before it freezes. This approach is employed to design an ice-resistant polymer nano-composite coating.

2.3 Numerical Simulation Techniques

There are several different numerical methods available for computing flows with moving interfaces: the level set method [39], [51], [53], the front tracking method [57], the lattice-Boltzmann method [23], [25], [36], [50], and the volume of fluid (VOF) method [29].

2.3.1 Volume of Fluid (VOF)

The VOF method is a numerical technique used to track the fluid-fluid interface in computational fluid dynamics [7]. It is suitable for simulations of droplet spreading on a surface because of its inherent mass conservation property. It is also appropriate for problems with topology changes and reduces computational costs. Though it is less accurate in interface calculations than the level set and front tracking methods, it is still the preferred method [29]. Hirt [29] also notes that using several points in a cell to define the region occupied by a fluid is unnecessarily excessive. The VOF method uses a volume fraction to define a fluid phase in each computational cell. A value of unity indicates the cell is completely occupied by the specified phase, a value of zero indicates the absence of the phase, and a value between zero and unity indicates the presence of the interface between the phases. The motion of a moving interface is predicted using an advection equation for the volume fraction of the tracked phase.

2.4 Water Droplets Impacting a Dry Surface

Many engineering applications require an understanding of the phenomenon of droplet impact and spreading on a dry surface. The mechanisms that control this phenomenon are diverse and heavily depend on the wettability and roughness of the. This topic has been studied extensively, but remains a topic of ongoing research [17], [47]. Rioboo *et al.* [46] identify six possible droplet spreading scenarios: deposition, prompt splash, corona splash, receding break-up, partial rebound, and complete rebound. The studies of Rioboo [44] demonstrated that impact on a dry surface will give rise to an expanding ejected liquid sheet, or lamella. The first two phases, deposition or prompt splash, can be thought of as precursors of the remaining four outcomes. Rioboo *et al.* [47] also noted that the deposition of the droplet on a dry, solid surface can be divided

into two phases. In the first, or kinematic, phase, the radius of the droplet contacting the surface is independent of the fluid or solid properties. However, in the second, or deposition, phase, the fluid and surface properties become important. After the droplet impacts the surface, the kinetic energy is dissipated by the action of viscous forces between the solid surface and the liquid or converted into surface energy resulting from the increase of surface area as the droplet spreads. The resulting morphology depends on available kinetic energy and surface characteristics, which can be described in terms of a contact angle, θ, which is defined as the angle between the wall and the tangent to the interface at the wall, measured inside the drop. In general, there is a hysteresis effect that produces an advancing contact angle, θ_A, and a receding contact angle, θ_R, with $\theta_R < \theta_A$ as shown in Figure 2.3.

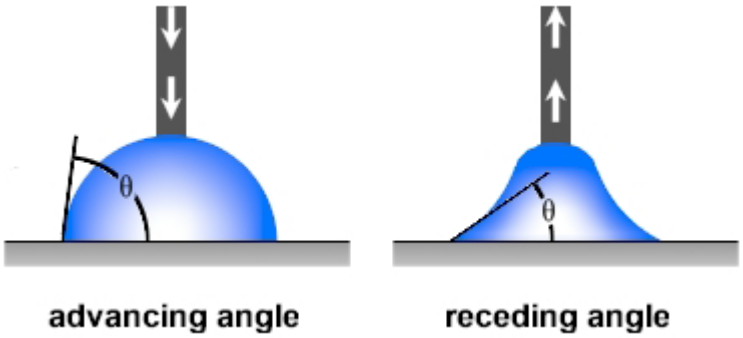

Figure 2.3 Advancing and receding contact angle hysteresis [27]

These phenomena are partially described by several nondimensional parameters [60]. The Reynolds number *Re* and Weber number *We*, given by

$$Re = \frac{\rho V_o D}{\mu} = \frac{\text{inertial forces}}{\text{viscous forces}} \tag{2.1}$$

and

$$We = \frac{\rho V_o^2 D}{\sigma} = \frac{\text{inertial forces}}{\text{surface tension}} \tag{2.2}$$

respectively, can be combined to obtain the Ohnesorge number *Oh*, which is given by

$$Oh = \frac{\mu}{(\rho\sigma d)^{1/2}} = \frac{We^{1/2}}{Re} = \frac{\text{viscous forces}}{\sqrt{interial\ forces\ x\ surface\ tension}}. \quad (2.3)$$

Larger values of *Oh* indicate that viscous effects are more important. Note, that none of these nondimensional parameters contain information about the properties of the surface upon which the droplets impact and, therefore, cannot fully describe the associated phenomena.

There have been a large number of studies reported in literature where numerical simulation has been employed to predict droplet impact on a dry surface. Only a representative sampling is discussed below. Fukai *et al.* [20] solved the Navier-Stokes equations with a finite element approach to simulate spreading of a droplet on a dry, partially wettable surface. The boundary condition applied at the contact line constrained its motion to be parallel to the surface. Fukai *et al.* [19] improved on this approach by applying the constant values for advancing and receding angles at the contact line as appropriate. This modification improved results when compared with experimental data. Gunjal *et al.* [24] simulated droplet impact on a solid, dry surface for a range of Reynolds and Weber numbers using Fluent 6.0, an earlier version of ANSYS Fluent 12.0. A time-varying dynamic contact angle (DCA), obtained from experimental data, was employed by prescribing a piecewise constant value of the contact angle for the given time intervals. Their results were able to capture key features of the droplet-surface interaction. Lunkad *et al.* [33] performed VOF simulations for droplet impact on horizontal and inclined surfaces. Their results were obtained using time-accurate variations of the contact angle obtained from experimental data [52] and suggested that accurate DCA specification is necessary for wettable surfaces, while less accuracy is

needed for less wettable surfaces. Roisman *et al.* [48] developed a model for the contact angle as a function of the instantaneous velocity of the contact line. Results predicted using a VOF solver showed good agreement with experimental data at low Weber numbers.

2.5 Water Droplets Impacting a Wet Surface

From a phenomenological standpoint, droplets impacting a wet surface versus a dry surface are drastically different, as discussed by Rioboo *et al.* [44]. Much effort has been expended to comprehend the underlying mechanisms of a droplet impinging a thin liquid film on a solid surface [14], [32], [45], [58], [60] including pre-existing liquid films, or films created by impacts of previous droplets. Droplet impact on a wetted surface produces a crown, i.e., splashing, though the break up process is widely varied and dependent on the thickness of the wet film as well as the film thickness relative to the mean surface roughness [60]. Mundo *et al.* [35] investigated the deposition and splashing limits as a function of Reynolds and Ohnesorge numbers for droplet impacts. The splashing was found to be nearly independent of the contact angle. The fact that the contact angle is not relevant in cases of droplets impacting a wetted surface to some extent simplifies the case in comparison to droplets on a dry surface. According to Mundo *et al.* [35], when the film on the surface is very thin, viscous effects from the wall can affect behavior after impact.

The effect of the film thickness on a surface has been studied through experiments and numerical simulations for a wide range of applications. Splashing is a common behavior observed when a droplet impacts a wetted surface. A high velocity impact of a single droplet onto a thin pre-existing film was considered by Cossali *et al.* [14] who

categorized the evolution of splash into four phases: crown formation and jetting, rim instability and jet formation, break-up of the jets and formation of secondary droplets, and crown collapse periods. A behavior commonly observed during the crown formation is fingering, or secondary droplets. The phases can be predicted and better understood using the same nondimensional parameters used to describe the behavior of a droplet impacting a dry surface, namely the Weber, Ohnesorge, and Reynolds numbers. Further, based on evaluation of these nondimensional numbers for various cases, Cossali *et al.* [14] concluded that a higher Weber number leads to the splash phenomenon during impact. Rioboo *et al*. [45] introduce an additional parameter, the dimensionless film thickness, H^*, defined as the ratio of the film thickness, h_0, to the drop diameter, d. They used a combination of Weber and Ohnesorge numbers as a function of dimensionless film thickness to describe the various phenomena that occur during liquid drop impact on a wetted surface. Their experimental investigation of splash and crown formation during the impact of a single droplet on a wetted surface demonstrated that for very thin film thicknesses, the crown formation was not evident. Wang *et al.* [58] showed that when the Weber number is increased, the fingering rim of the crown formed during the early stage may scatter into many satellite drops. The impact of a single drop on a liquid film was studied numerically by Rieber *et al.* [43] by solving the Navier-Stokes equations for incompressible fluids by the VOF method. Physically realistic results showed crown formation with outward propagation.

CHAPTER III

COMPUTATIONAL METHODS

3.1 Flow Solver

The numerical simulations were performed using OpenFOAM® 2.0 (Open Field Operation and Manipulation) [38]. OpenFOAM® CFD, a C++ toolbox, is a free, open-source CFD software package produced by OpenCFD Ltd [37]. The package has an extensive range of features to solve problems from complex fluid flows involving chemical reactions, turbulence and heat transfer, to solid dynamics and electromagnetics. Tools for meshing, pre- and post-processing are also included. Because it is open source, the code offers users complete liberty to tailor and broaden its functionality. OpenFOAM® employs a highly modular strategy in which collections of functionality (numerical methods, meshing, physical models, etc.) are each compiled into their own shared library. Executable applications are created and are linked to the various OpenFOAM® libraries.

OpenFOAM® has the capability to perform simulations for two immiscible fluids impacting a dry surface using a volume of fluid (VOF) [17] approach using the module InterFoam [29]. InterFoam is based on the two-fluid approach developed by Rusche [49] and later modified by OpenCFD Ltd. [37]. The approach is described in detail by Berberovic *et al*. [5]. In the two-fluid approach, phase fraction equations are solved for each phase [12] to ensure boundedness and conservation. This is crucial to realize an

accurate solution, especially for problems in which the densities of the two phases are widely different, e.g., water and air.

Domains considered in the present simulations were generated using the *blockMesh* utility [38]. For the axisymmetric domains, the flow domain considered has the form of a wedge with only one cell in the azimuthal direction. The grid was manually refined in the region where droplet impact takes place. Three-dimensional simulations were performed using a quarter-plane symmetry technique in order to reduce simulation time in which computations are performed in only one quarter of the domain.

3.2 Governing Equations

The governing equations, continuity and momentum,

$$\nabla \cdot \boldsymbol{u} = 0 \tag{3.1}$$

$$\frac{\partial(\rho V)}{\partial t} + V \cdot (\rho V V) = -\nabla p + \nabla \cdot T + \rho f_b \tag{3.2}$$

are solved simultaneously with the transport equation for an indication function, representing the volume fraction of one phase

$$\frac{\partial \alpha}{\partial t} + \nabla \cdot (V\alpha) = 0 \tag{3.3}$$

The code utilizes a cell-center-based finite volume method on a fixed, unstructured numerical grid. Coupling between pressure and velocity in transient flows is done using the pseudo-transient PIMPLE algorithm, which is a hybrid based on the pressure-implicit split-operator (PISO) and semi-implicit method for pressure-linked equations (SIMPLE) algorithms [5], [30]. The InterFoam solver uses the multidimensional universal limiter for explicit solution (MULES) method, created by OpenCFD, to preserve boundedness of the phase fraction autonomous of underlying numerical scheme, mesh structure, etc. [5]. The selection of schemes for convection is consequently not restricted to those that are

strongly stable or bounded, such as upwind differencing [38]. The equations are discretized following the finite-volume technique. The transient and source terms are discretized using the midpoint rule and integrated over cell volumes. Time derivative terms are discretized using a first-order, bounded, implicit Euler scheme and terms containing spatial derivatives (diffusion and convective terms) are converted into integrals over surfaces bounding each cell with Gauss' theorem, a second-order Gaussian integration. Obtained by interpolation, integration is performed by summing the values at the cell faces. Gradients are evaluated with a linear (central differencing) face interpolation. A diagonal incomplete-Cholesky (symmetric) (DIC) preconditioned conjugate gradient (PCG) solver is used to precondition the pressure equation [4]. The momentum matrix is smoothed using a diagonal incomplete-LU (asymmetric) (DILU) PCG preconditioner and solved with a preconditioned bi-conjugate gradient (PBiCG) solver [4].

3.3 Volume of Fluid Implementation

The governing equations are modeled via the VOF approach [17]. Here, the air is taken to be the primary phase and the liquid (water) to be the secondary phase. The secondary phase is defined in terms of a volume fraction, α_s, in each computational cell:

$\alpha_s = 0$ the cell does not contain the secondary phase
$\alpha_s = 1$ the cell contains only the secondary phase
$0 < \alpha_s < 1$ the cell contains the interface between the primary and secondary phases

The value of α_s is obtained by solving the convection equation, Equation (3.3). The volume fraction of the primary phase is then given by

$$\alpha_p = 1 - \alpha_s. \tag{3.4}$$

To ensure boundedness and conservation, a modified convection equation is solve

$$\frac{\partial \alpha_s}{\partial t} + \nabla \cdot (V\alpha_s) + \nabla \cdot [V_r \alpha_s (1 - \alpha_s)] = 0 \tag{3.5}$$

where V_r represents the relative velocity between the two phases. The additional convection term, which is only active near the interface, is referred to as the "compression term" and, with appropriate discretization, significantly reduces the smearing that occurs at the interface in traditional VOF techniques. A model for V_r is required to provide closure for the system. As described in Berberovic *et al*. [5], the relative velocity at a cell face is based on the velocity through the face, the gradients of the phase fraction, and the maximum velocity magnitude in the interface region. A compression parameter is included that can be used to further sharpen the interface.

3.4 Model for Contact Line Motion

The impact of a droplet on a dry surface is rife with complexity. In the approach employed in InterFoam, a single momentum equation is solved that accounts for the effects of surface tension, which is shown in Equation (3.2). One effect of the surface tension at the interface between the phases is the generation of a phase gradient that is accounted for via the body force term f_b, which is evaluated with the continuum surface force model of Brackbill *et al.* [7],

$$f_b = \sigma \left[-\nabla \cdot \left(\frac{\nabla \alpha_s}{|\nabla \alpha_s|} \right) \right] \nabla \alpha_s \tag{3.6}$$

where the term in parentheses represents the normal to the interface and the term in square brackets represents the curvature of the interface. If a direct numerical simulation of the moving interface is desired, requiring resolution of all necessary spatial scales, the computation would be intractable [52]. This difficulty can be circumvented by modeling

the effects of the near wall region with a modification of the normal to the contact line, i.e., the normal to the interface, by modifying the normal to the interface

$$\left(\frac{\nabla\alpha_s}{|\alpha_s|}\right)_{mod} = n_{wall}cos\theta + t_{wall}sin\theta \tag{3.7}$$

where θ is the contact angle, in this case, prescribed by experimental data or obtained from an appropriate model.

In the InterFoam solver of OpenFOAM® 2.0, the contact angle is computed using the following heuristic:

$$\theta = \theta_0 + (\theta_A - \theta_R) \times \tanh\left(\frac{u_{wall}}{u_\theta}\right). \tag{3.8}$$

Here, u_{wall} is an estimate of the contact line velocity based on the velocity of the fluid parallel to the wall "near" the contact line defined so that a positive quantity indicates an advancing contact line. However, as noted by Sikalo *et al.* [52], the fluid velocity in a region very near the wall is not representative of the velocity of the contact line. The rationale is that the hyperbolic tangent function will transition smoothly between a "larger" value and a "smaller" value of the DCA while running the static contact angle (SCA) when u_{wall} is zero, i.e., the contact line is stationary. The scaling parameter u_θ is responsible for the rapidity of this transition.

Unfortunately, as formulated, the above equation returns neither the advancing nor the receding contact angles at its extremes. To address this issue, a new function was implemented in the InterFoam solver

$$\theta = \theta_0 + (\theta_A - \theta_0) \times \tanh\left(\frac{u_{wall}+|u_{wall}|}{2u_\theta}\right) + (\theta_R - \theta_0) \times \tanh\left(\frac{u_{wall}-|u_{wall}|}{2u_{wall}}\right) \tag{3.9}$$

When u_{wall} has a positive value, which represents an advancing contact line, the last hyperbolic tangent function will return 0 and $\theta=\theta_A$. Likewise, when u_{wall} is negative, for a receding contact line, the first hyperbolic tangent function returns 0 and $\theta=\theta_R$.

Although this function accommodates the transition between advancing and receding contact angles (droplet oscillation), this equation is still a heuristic and acceptable values of u_θ must be determined on a case by case basis. In general, small values of u_θ will ensure the proper contact angle is being used. This function is correctly viewed as a mechanism for automatically switching between constant values of the advancing, static, and receding contact angles based on interface motion. Fortunately, as noted by Sikalo *et al*. [52], accurate specification of the DCA is less critical for hydrophobic and superhydrophobic surfaces than for hydrophilic surfaces. It should be noted that no significant differences were observed in results predicted using Equations (3.8) and (3.9).

CHAPTER IV

RESULTS

In this section, results predicted using InterFoam are compared with numerical results and experimental data. The cases included in the validation effort are listed in Table 4.1 and represent droplet impact on hydrophobic surfaces. These cases represent a range of Reynolds and Weber numbers. Data for comparison for Case I, in which a glycerin droplet impacts a wax-coated surface, was obtained from Lunkad *et al*. [33] and Sikalo *et al*.[52]. The experimental data for Case II, in which a water droplet impacts a hydrophobic surface formed by a smooth polyurethane coating, was obtained by Jung and Raps at EADS-IW [41]. Additional results presented simulate droplet impact on an airfoil under near flight conditions on a micron-scale domain to understand the effects of a water film, representing a saturated surface in high humidity conditions, on the hydrophobicity of a surface with micro-scale roughness elements (MRE).

4.1 Validation

Table 4.1 Relevant parameters for the droplet impact cases discussed in Section 4.1.

	Liquid	Diameter, *mm*	Static contact angle θ_0	Advancing contact angle θ_A	Receding contact angle θ_R	Impact velocity $m\text{-}s^{-1}$	*Re*	*We*	*Oh*
Case I	Glycerin	2.450	93.5°	N/A	N/A	1.036	4.003	52.6	1.812
Case II	Water	2.673	93±3°	98±2°	77±3°	0.979	2604	35.1	0.0023

4.1.1 Case 1: Glycerin Droplet Impacting a Wax-coated Surface

The first case considered is a glycerin droplet, with a diameter of 2.45 *mm,* impacting a wax-coated hydrophobic surface at a velocity of 1.036 *m/s* [33], [52]. InterFoam was used to perform simulations for this case on uniform meshes at resolutions of 10 and 20 cells per radius (CPR) in a 12.5 *mm* by 12.5 *mm* domain. A spherical droplet with a vertical velocity was introduced at a distance of 0.275 *mm* above the surface. The no-slip boundary condition was applied on the wall boundary and a constant-pressure, inlet/outlet boundary condition was applied to the top and side boundaries. A constant SCA of 93.5° was employed. In this case, a variable time step was employed that was adjusted according to the algorithm described by Berberovic *et al.* [5] to maintain stability. Results were saved at intervals of 1 *ms*. Figure 4.1 shows the droplet shape at various times after impact compared with the images from Lunkad *et al.* [33]. The shape of the droplet shows good agreement with the numerical results. Figure 4.2 shows a quantitative comparison between the time histories of the droplet height and width computed by InterFoam and the data from Sikalo *et al.* [52]. The maximum spreads predicted by InterFoam were 1.992 and 2.035 droplet diameters for the 10 CPR and 20 CPR meshes, respectively, which represents an over prediction relative to the data from Sikalo *et al.* of approximately 25%. This trend was observed in all of the results produced by InterFoam. The differences between the results on the two meshes are not significant and indicate that the 20 CPR mesh provides adequate spatial resolution for this simulation.

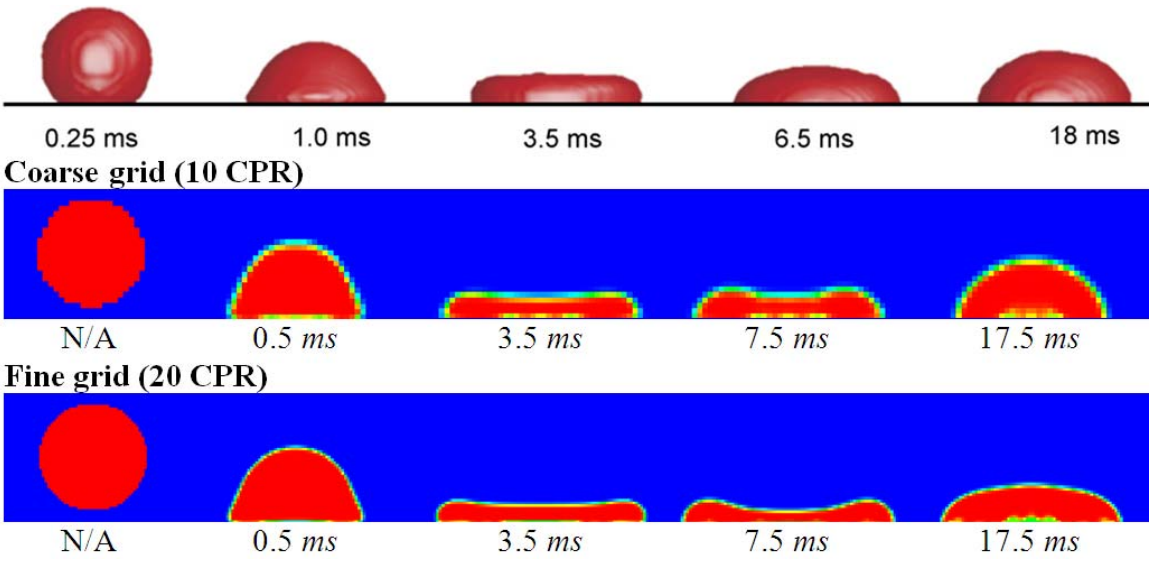

Figure 4.1 Qualitative mesh refinement results for InterFoam. Case I: Glycerin droplet impacting a hydrophobic surface at a velocity of 1.036 *m/s* with a SCA of 93.5°. Times listed for results are approximate and are referenced to an estimated time of impact. The top image shows numerical results taken from Lunkad *et al.* [33].

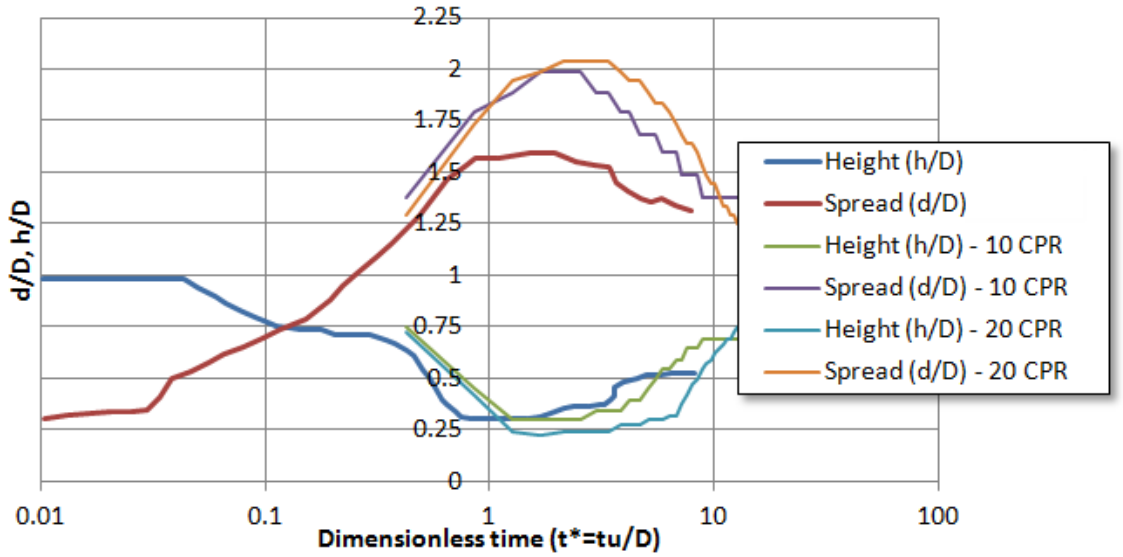

Figure 4.2 Quantitative mesh refinement results for InterFoam. Case I: Glycerin droplet impacting a hydrophobic surface at a velocity of 1.036 *m/s*. SCA of 93.5°. Experimental data taken used for comparison was taken from Sikalo *et al*. [52].

4.1.2 Case II: Water Droplet Impacting a Hydrophobic Surface

Case II represents a spherical 10 μl (2.673 *mm* diameter) water droplet released from a height of 5 *cm* impacting a hydrophobic, smooth polyurethane coated surface. Released from this height, the droplet impacts the surface at approximately 0.979 *m/s*. Experimental data was obtained for this case by personnel at EADS-IW [42]. Results of the experiment are shown in Figure 4.3, in which the dimension indicated on the scale is in *mm*. The first image shows the droplet before impact, the second image shows the maximum spread of the droplet, and the third image shows the droplet after retraction.

Simulations of this case were performed using InterFoam with the DCA as modeled using Equation (3.9). For comparison, axisymmetric droplet impact simulations were also performed using a VOF implementation with ANSYS Fluent 12.0 [18]; however, Fluent did not accurately capture the physical behavior of droplet impact for this case.

4.1.2.1 Axisymmetric Simulations

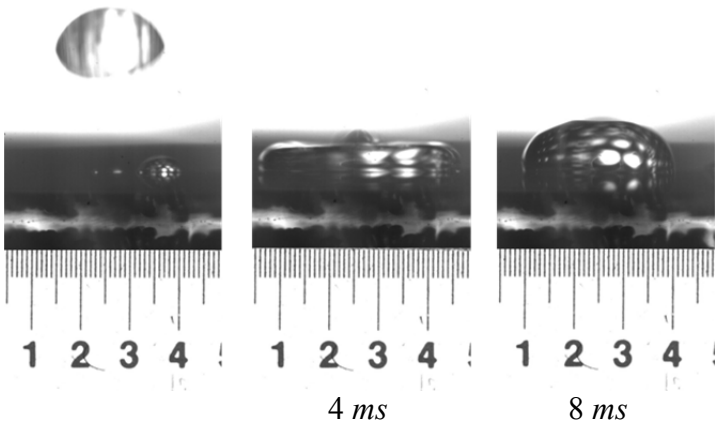

Figure 4.3 Experimental results [42]: 10 μl droplet impact from 5 *cm* on smooth hydrophobic surface. Times shown are referenced to the time of droplet impact.

The computational domain used for this case was a 17.37 *mm* by 60.14 *mm* rectangular region. Grid resolution effects were studied with a comparison of simulations for uniform meshes with 10, 20, and 40 CPR. The no-slip boundary condition was specified at the wall and the domain was axisymmetric. Since the flow conditions were not known at the top and outside faces, they were assumed to be constant-pressure, inlet boundaries. A variable time step was used. The simulations were performed using a DCA defined by Equation (3.9) with $\theta_A = 98°$, $\theta_R = 77°$, $\theta_0 = 93°$, and u_0=0.01. To initialize the simulation, a spherical droplet was introduced at a distance of 5 *cm* above the surface with no vertical velocity, allowing the droplet velocity to develop in response to the gravitational and drag forces. The observed droplet impact velocity is consistent with results obtained from a 4^{th}-order Runge-Kutta integration [9] of the rigid body equations of motion for the velocity of the droplet at impact. To reduce the cost, the computational domain was discretized using a uniform 5 CPR and refined in an L-shaped region (along the axis of symmetry and the wall) to 10, 20, and 40 CPR. The 40 CPR domain and refinement are shown in Figure 4.4.The maximum spread of the droplets was compared for each domain as shown in Figure 4.5. It was observed that results predicted using the 40 CPR domain demonstrated the best agreement with experimental results in terms of maximum droplet spread. Although agreement with experimental data improved as the mesh was refined, all meshes showed an over prediction of the spread.

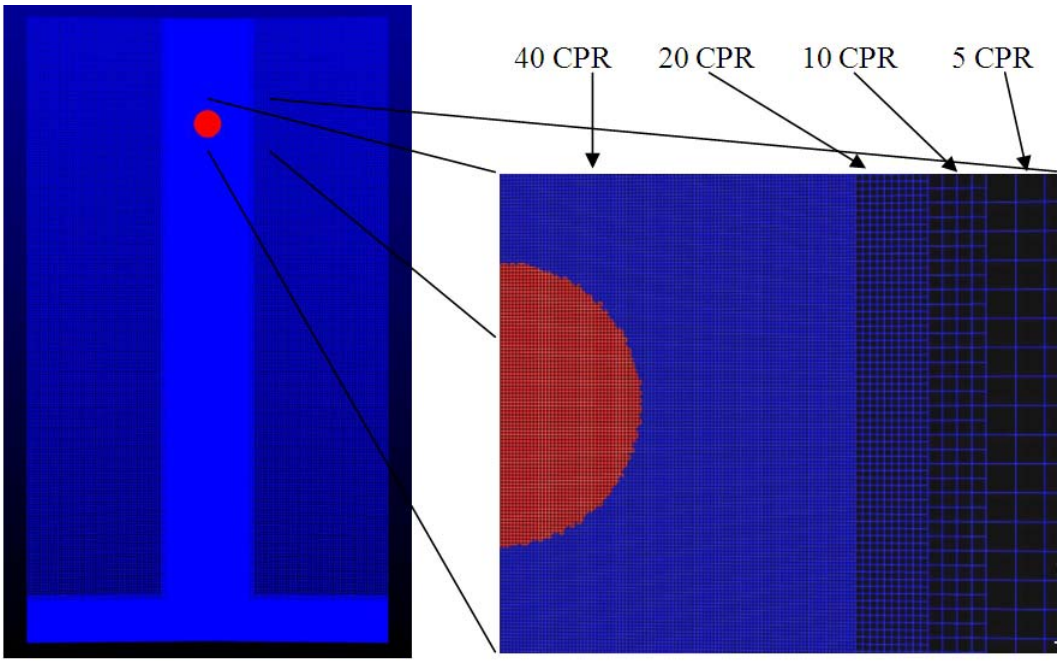

Figure 4.4 (a) Axisymmetric 37 *mm* by 60.14 *mm* rectangular domain showing L-shaped refinement. (b) Close view of droplet showing refinement transition from 40 CPR to 5 CPR

To further decrease computational expense, the effect of specifying the droplet velocity as opposed to allowing it to develop as the droplet falls from a 5 *cm* height was explored. The droplet was initialized 2.34 *mm* above the surface and a uniform velocity of 0.979 *m/s* was specified. This allowed for reduction of the domain in the vertical direction. The axisymmetric domain was 17.37 *mm* x 17.37 *mm* with an L-shaped refinement to 20 CPR, as previously described, and 5 CPR elsewhere. The qualitative results for maximum spread are shown in Figure 4.6. Figure 4.7 shows a quantitative comparison between the time histories of the droplet width as computed by InterFoam for the mesh refinement study. The case in which a specified velocity was employed resulted in an over-prediction of the maximum spread. This is likely due to the influence

of the air below the droplet as it falls as well as secondary currents within the droplet. Simulations on a two-dimensional domain showed behavior of the droplet that was very comparable to the axisymmetric results. Simulations were also performed on a domain which was generated by applying stretching in the *y*-direction, normal to the wall, to an axisymmetric, uniform 10 CPR mesh, resulting in cells clustered near the wall. The expansion ratio of the last cell to the first was 10:1. It was apparent that the droplet becomes elongated before impact to the stretched mesh. This was attributed to the anisotropic cells in the stretched mesh. This result suggests that the most reliable results from the InterFoam VOF algorithm are obtained on isotropic meshes.

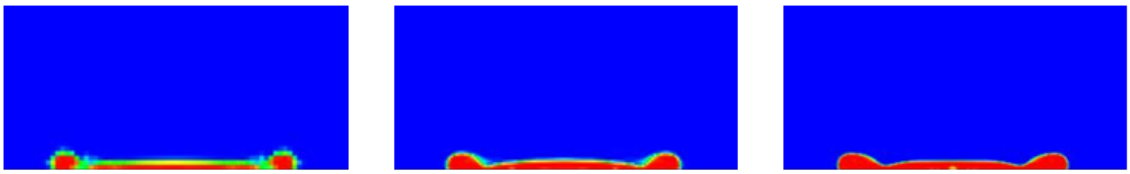

10 CPR
6.682 *mm*

20 CPR
5.88 *mm*

40 CPR
5.614 *mm*

Figure 4.5 Qualitative axisymmetric mesh refinement results for InterFoam. Case II: 10 μl water droplet impacting a hydrophobic surface at a velocity of 0.979 *m/s* with a SCA of 93.5°. Images shown are maximum spread of droplet after impact.

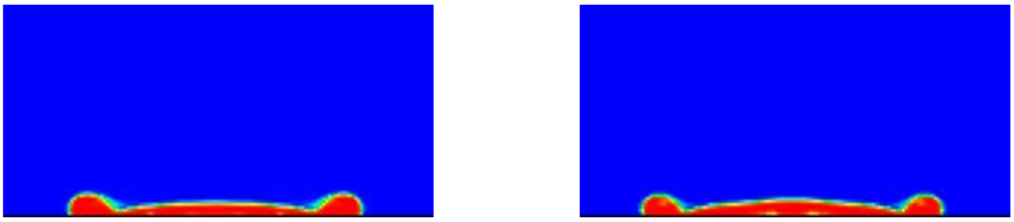

20 CPR, "free fall" from 5 *cm*
5.88 *mm*

20 CPR, specified velocity of 0.979 *m/s*
6.934 *mm*

Figure 4.6 Qualitative axisymmetric results for InterFoam comparison of maximum spread in *mm* for "free fall" and specified velocity. Case II: 10 μl water droplet impacting a hydrophobic surface at a velocity of 0.979 *m/s* with a SCA of 93.5°. Images shown are maximum spread of droplet after impact.

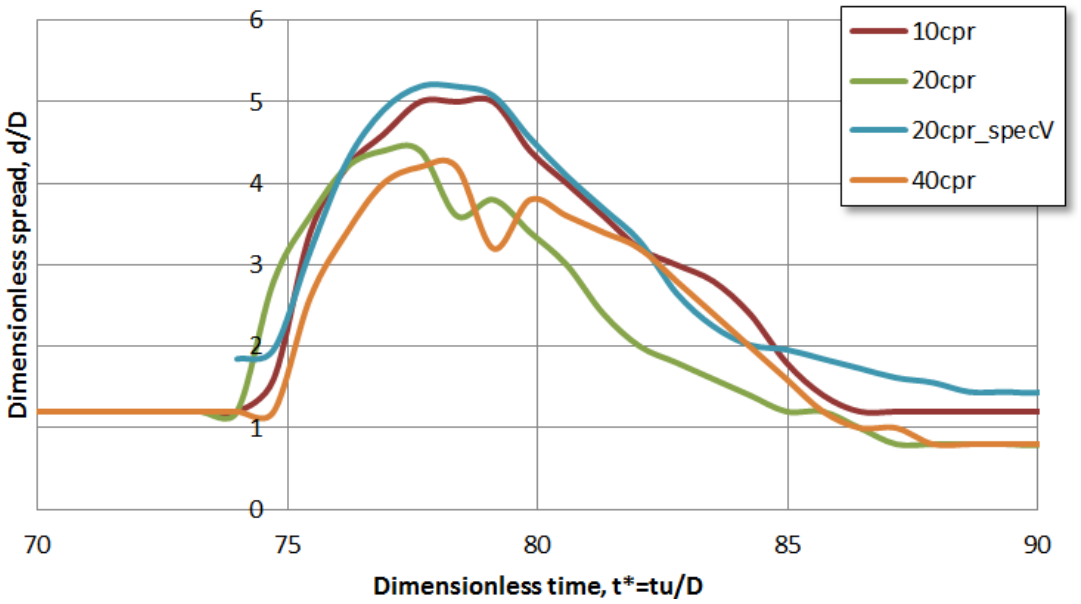

Figure 4.7 Quantitative mesh refinement results for InterFoam. Case II: 10 μl water droplet impacting a hydrophobic surface at a velocity of 0.979 *m/s*.

Images in a video obtained during the experiment indicate that the droplet shape near impact is elliptical rather than spherical. The effects of droplet shape were investigated to see if agreement with experimental data could be improved using the same domain and initial conditions, but with an elliptical 10 μl droplet (semi-major axis of 1.54 *mm* and semi-minor axis of 1.16 *mm*) initialized 5 *cm* above the surface with no vertical velocity specified. Simulations were performed with uniform 10 and 20 CPR domains. The numerical simulations for an elliptical droplet demonstrated a significant over-prediction of the maximum spread after impact as compared to the measured value of 3.662 *mm* from the experimental data, shown in Figure 4.8.

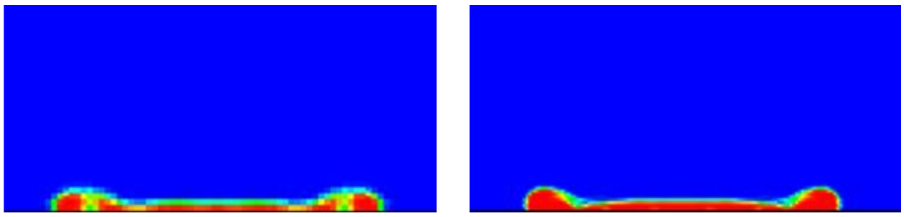

Figure 4.8 Qualitative mesh refinement results for InterFoam for elliptical droplet. Case II: 10 μl water droplet impacting a hydrophobic surface at a velocity of 0.979 *m/s* with a SCA of 93.5°. Images shown are maximum spread of droplet after impact.

In all cases, the results for the retraction phase of the simulation did not agree with the experimental results and were not consistent for the 10 and 20 CPR domains. In the simulations using the 10 CPR mesh, the droplet separated into annular regions before agglomerating as retraction proceeded. The 20 CPR simulation does not exhibit this behavior. In this case, the droplet advanced and began to retract as a single droplet. All simulations depicted a lamella that formed on the outer edge of the droplet as it expanded across the surface after impact, which is consistent with the experimental data. Figure 4.9 shows the droplet 15 *ms* after impact when it is well into the retraction phase. On the uniform 10 CPR domain, the droplet retracted and rebounded. The uniform 20 CPR case remained a single droplet as it rebounded off the surface and impacted a second time. It is evident that the physics of the droplet during retraction are not accurately simulated and require further investigation.

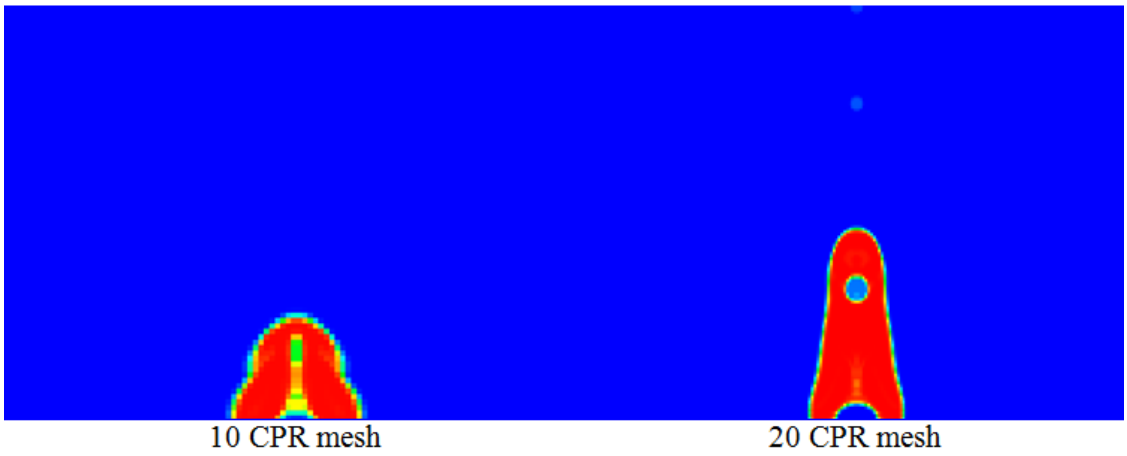

Figure 4.9 Retraction at 15 *ms* from first contact. Case II: Water droplet impacting a hydrophobic surface at a velocity of 0.979 *m/s* with DCA.

4.1.2.2 Three-Dimensional Simulations

Additional simulations for Case II were performed on a three-dimensional domain. A domain of 34.7 *mm* x 60.1 *mm* x 34.7 *mm* was utilized, with a uniform 10 CPR mesh resolution. Boundary conditions remained the same as previous simulations. The 10 μl droplet was initialized 5 *cm* above the surface and allowed to fall under the influence of drag and gravity. The maximum spread for the three-dimensional simulation is shown in Figure 4.10. The maximum spread of the droplet after impact was compared to the 10 CPR axisymmetric results. The observed behavior of the spread and recoil for axisymmetric and three-dimensional simulations was very similar. The three-dimensional simulations demonstrated a maximum spread approximately 1 *mm* larger than the axisymmetric simulation. This is not completely surprising since the three-dimensional mesh may not be as effective representing the droplet and its impact as an axisymmetric mesh with a similar discretization.

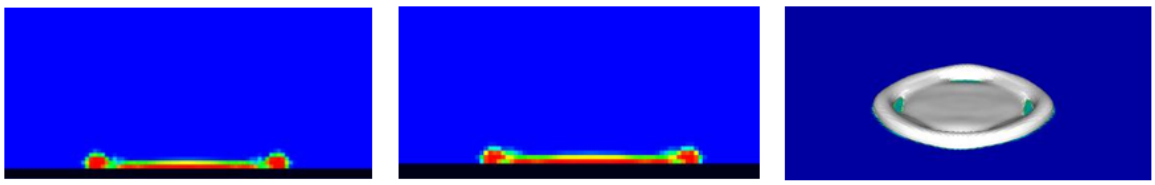

Axisymmetric, 10 CPR
6.682 mm

Three-dimensional, 10 CPR (cross section and iso view)
7.531 *mm*

Figure 4.10 Qualitative mesh refinement results for InterFoam for droplets with 10 CPR in axisymmetric and three-dimensional simulations. Case II: 10 μl water droplet impacting a hydrophobic surface at a velocity of 0.979 *m/s* with a SCA of 93.5°. Images shown are maximum spread of droplet after impact.

4.2 Structured MRE for Aircraft Icing Applications

A common theme of superhydrophobic surfaces is the geometric properties of nano-scale roughness which reduce the surface area a droplet encounters. Mishchenko [34] suggest micro-structured, superhydrophobic surfaces for the development of anti-icing materials. The results of their studies found that nano- and micro-structured materials induce complete retraction of impacting water droplets prior to the occurrence of ice nucleation and may provide an effective strategy to prevent ice formation. When an aerodynamic surface is in high humidity conditions, in the presence of visible moisture, a thin film of water is present on the surface. This thin film may cause a degradation in the ability of the micro-structures to repel water. The effect of micro-scale roughness elements (MREs) under dry and high humidity conditions are investigated for aircraft icing applications.

4.2.1 Approach

Simulation of droplets impacting an aerospace vehicle under flight conditions is an inherently multi-scale problem. The flow around the vehicle occurs on a scale on the order of meters while the droplet scale is on the order of microns, and the surface-droplet

interactions occur at the atomistic scale. To a micron-scale droplet, the region near a stagnation point on a symmetric airfoil at zero angle of attack appears very similar to the stagnation point on a cylinder. The radius of this cylinder is equivalent to the leading-edge radius for the airfoil, which is included in NACA airfoil definitions [1]. This observation provides a mechanism to couple the macro-scale flow field to the micron-scale droplet flow field. Using a potential flow solution for flow near a stagnation point on a cylinder of radius *R,* shown in Figure 4.11, the velocity of a droplet at a specified distance *d* before impact can be computed.

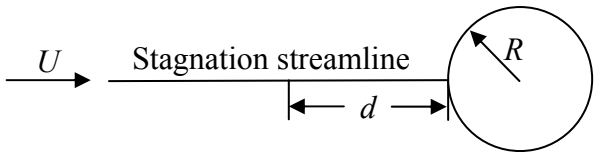

Figure 4.11 Flow near a stagnation point on a cylinder of radius *R*.

The stream function for the corresponding inviscid, irrotational flow is given by [6]

$$\phi = U_\infty r sin\theta \left(1 - \frac{R^2}{r^2}\right) \tag{4.1}$$

and

$$u_r = U_\infty cos\theta \left(1 - \frac{R^2}{r^2}\right) \tag{4.2}$$

Along the stagnation streamline, i.e., $\theta = \pi$, the horizontal velocity component—positive direction is taken to the right—is given by

$$u_{flow} = U_\infty \left(1 - \frac{R^2}{r^2}\right) \tag{4.3}$$

which can be defined as a function of the distance *d* from the stagnation point as

$$u_{flow}(d) = U_\infty \left(1 - \frac{R^2}{(R+d)^2}\right). \tag{4.4}$$

Neglecting buoyancy ($\rho_{air} << \rho_{droplet}$) and Saffman lift, the one-dimensional equation of motion for a particle moving along the horizontal axis is given by

$$m_{droplet}\frac{du}{dt} = D_{droplet} \tag{4.5}$$

where u is the horizontal component of droplet velocity and $D_{droplet}$ is the horizontal component of the drag force acting on the droplet. Rewriting Equation (4.5) using the definition of the drag coefficient yields [15]

$$m_{droplet}\frac{du}{dt} = \frac{1}{2}\rho_{air}\left|u_{flow}(d) - u\right|\left(u_{flow}(d) - u\right)AC_D \tag{4.6}$$

where A is the projected area of the assumed spherical droplet, u_{flow} is the flow velocity given in Equation (4.4), and C_D is the drag coefficient for a sphere given by the curve fit of [13]

$$C_D = \frac{24}{Re_{rel}}\left(1 + 0.15{Re_{rel}}^{0.687} + 0.0175\left(1 + 42500{Re_{rel}}^{-1.16}\right)^{-1}\right) \tag{4.7}$$

which is a modification of the Stokes' solution to account for Reynolds number effects and is valid for $Re_{rel} < 350{,}000$. Re_{rel} is the relative Reynolds number for a sphere of diameter D given by

$$Re_{rel} = \frac{\rho_{air}\left|u_{flow}(d) - u\right|D}{\mu_{air}}. \tag{4.8}$$

The drag function in Equation (4.7) is a correlation over a wide range of Re_{rel} and provides a fit for C_D within ± 6% of the experimental value over this range [13].

The velocity of the droplet is computed by first specifying the initial position and velocity of the droplet in a region upstream of the cylinder in a region where the flow velocity is nearly the freestream velocity, and integrating Equation (3.2) using a 4th- order Runge-Kutta method [9]. For example, a 50 μm-diameter droplet located 200 μm above the surface with the top boundary of computational domain 400 μm above the surface, for

a NACA0012 airfoil with $R = 0.017\ m$ (17,000 μm), the computed velocities are shown in Table 4.2. Here, V_∞ is the freestream air velocity, V_{top} is the velocity at the top of the domain, $V_{droplet}$ is the velocity of the droplet, V_{rel} is the relative velocity between the droplet and the flow, and Re_{rel} is the relative Reynolds number.

Table 4.2 Computed velocity in *m/s* for 50 μm-diameter droplet located 200 μm above the surface.

V_∞	V_{top} at 400 μm	$V_{droplet}$ at 200 μm	V_{rel} at 200 μm	Re_{rel} at 200 μm
60	2.73	53.6	-52.2	200.5

Multiple simulations were performed to study the effect of a thin water film on the hydrophobicity of surfaces with structured MREs. A droplet velocity of 53.6 *m/s* was used for a 50 μm-diameter droplet impacting two different superhydrophobic surfaces: a smooth surface and a surface with 5 μm x 5 μm MREs. Simulations were performed using an axisymmetric domain to establish the mesh spacing and identify trends. It should be noted that the axisymmetric simulations cannot accurately describe the behavior of a droplet impacting a surface with MREs. Because the axisymmetric domain is a wedge, the simulated MREs actually represent concentric circles rather than parallel ridges on the surface. By performing a mesh refinement study on axisymmetric domains, the usefulness of three-dimensional simulations to evaluate the effectiveness of the MREs on the surface can be determined by obtaining information about droplet behavior on axisymmetric domains.

The relevant parameters for the droplet impact cases discussed in this section are shown in Table 4.3. Compared to the cases discussed in Section 4.1, this droplet is three

orders of magnitude smaller and impacts the surface at a significantly higher velocity. The nondimensional Reynolds number is comparable to Case II, however, the Weber number is much larger due to the increased velocity and decreased droplet diameter. This indicates that droplet behavior is driven primarily by inertial forces. Additionally, the Ohnesorge number is low. This implies that viscous effects are not as important for this case, and, recalling from results in Section 4.1, the simulations performed well for highly viscous cases (Case I). It is important to note that the nondimensional numbers do not take surface type into account and are strictly based on the fluid properties and velocity.

Table 4.3 Relevant parameters for the droplet impact cases discussed in Sections 4.2.2 and 4.2.3.

Liquid	Diameter, μm	Static contact angle θ_0	Advancing contact angle θ_A	Receding contact angle θ_R	Impact velocity $m\text{-}s^{-1}$	*Re*	*We*	*Oh*
Water	50	149±4°	154±3°	150±4°	53.6	2986	2461	0.0167

4.2.2 Droplet Impact on Smooth Surface

4.2.2.1 Dry Smooth Surface

Simulations performed on an axisymmetric domain for a 50 μm-diameter water droplet impacting a smooth, dry, superhydrophobic surface with a specified velocity of 53.6 *m/s* released from 200 μm above the surface are presented here. A 400 μm x 400 μm computational domain was used for these axisymmetric simulations with a uniform mesh refinement of 50 and 100 CPR. The maximum spread of the droplet after impact was measured and compared for each domain. The maximum spreads for the 50 and 100 CPR domains are shown in Figure 4.12 and Figure 4.13, respectively. The observed

maximum spreads were very similar on the two domains indicating that the 100 CPR resolution is adequate.

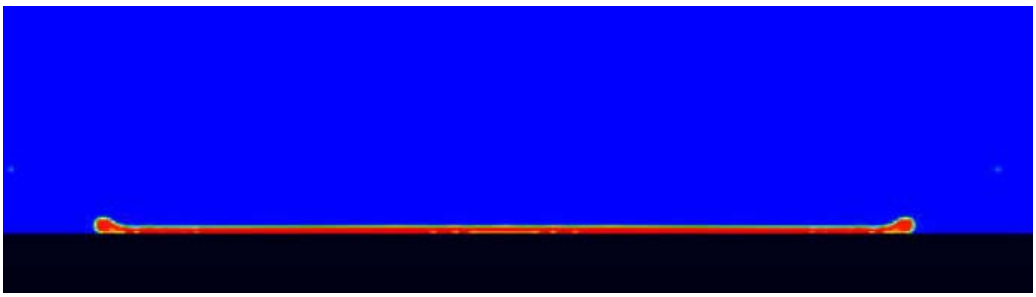

210.242 μm

Figure 4.12 Qualitative results for InterFoam on axisymmetric domain with 50 CPR for 50 μm-diameter droplet impacting smooth dry surface at 53.6 m/s.

209.906 μm

Figure 4.13 Qualitative results for InterFoam on axisymmetric domain with 100 CPR for 50 μm-diameter droplet impacting smooth dry surface at 53.6 m/s.

4.2.2.2 Thin Wet Film on Smooth Surface

The same case shown in Section 4.2.2.1 was used with a thin film of water on the surface, which is equivalent to a saturated surface in high humidity conditions. The thickness of the film on the surface was 5 μm. Simulations were performed on the same size domain with resolutions of 50 and 100 CPR. All boundary conditions remained the same, with the exception of the right boundary, which was specified to be *zeroGradient* in which the gradient normal to the boundary is taken to be zero. This allows fluid

reaching that boundary to exit with minimal reflection. Figure 4.14 and Figure 4.15 show the maximum spread of the droplet after impact on the 50 and 100 CPR domains. As in Figure 4.16, the four phases of splash evolution are shown in the simulation and are characteristic of a high velocity impact of a single droplet onto a thin pre-existing film [14].

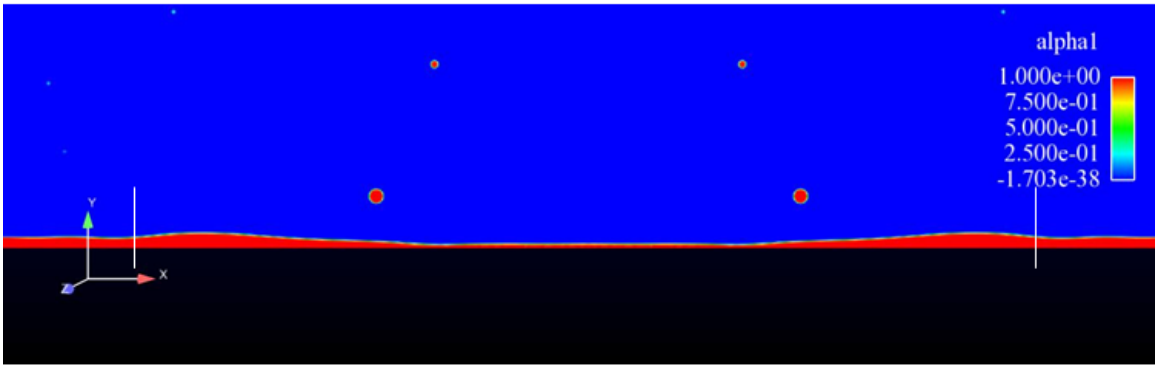

Figure 4.14 Qualitative results for InterFoam on axisymmetric domain with 50 CPR for 50 μm-diameter droplet impacting smooth wetted surface at 53.6 m/s. Film thickness on surface is 5 μm. The maximum spread is indicated with the white bars.

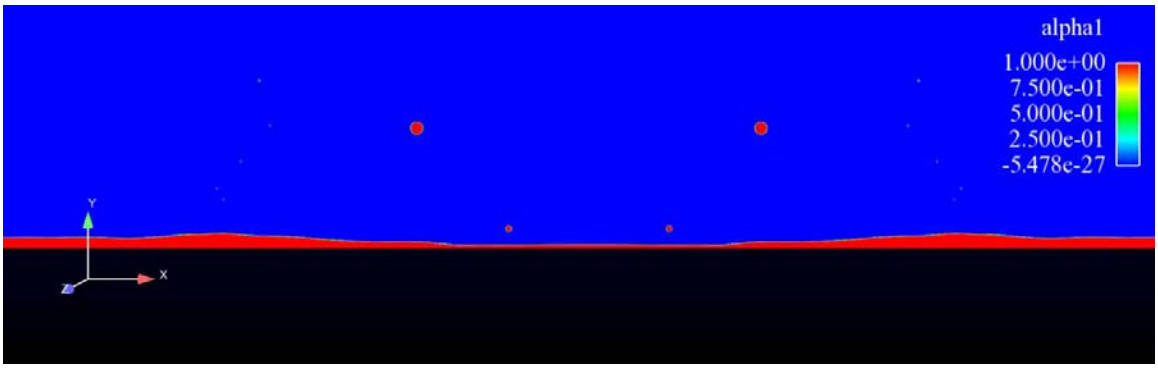

432.928 μm

Figure 4.15 Qualitative results for InterFoam on axisymmetric domain with 100 CPR for 50 μm-diameter droplet impacting smooth wetted surface at 53.6 *m/s*. Film thickness on surface is 5 μm. The maximum spread is indicated with the white bars.

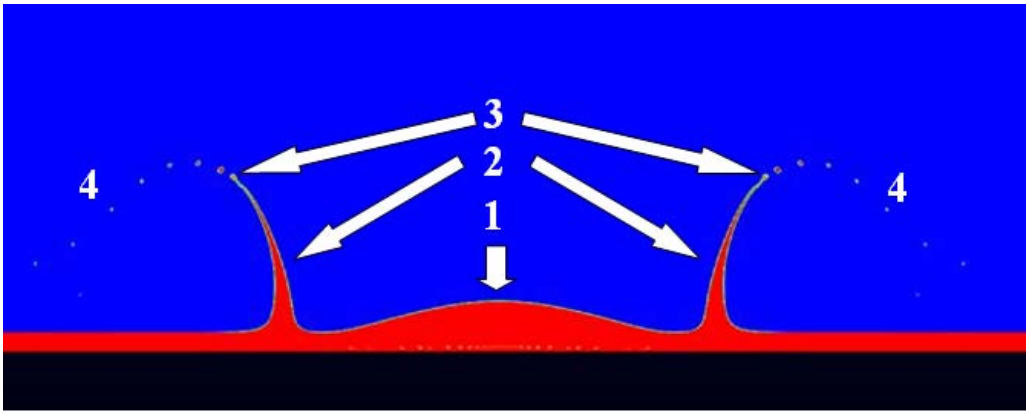

Figure 4.16 Splash mechanism demonstrated from results for InterFoam on axisymmetric domain with 100 CPR for 50 μm -diameter droplet impacting smooth wetted surface at 53.6 *m/s*. Film thickness on surface is 5 μm.

1. Residual top of impacting drop

2. Section of crown-like sheet propagating outward

3. Cross-section of free rim

4. Secondary droplets formed from cusps of free rim

4.2.3 Droplet Impact on a Surface with Structured MREs

4.2.3.1 MREs with Dry Surface

The same simulations were repeated for surfaces with structured MREs measuring 5 μm x 5 μm introduced on the surface. Due to the small size of the cavities between the MREs, it was determined that a more refined mesh would be necessary to resolve the behavior of the droplet impacting the surface. Two axisymmetric domains measuring 1900 μm x 2300 μm with resolutions of 100 CPR and 200 CPR were employed. The DCA superhydrophobic contact angle was specified on the MREs surface. The maximum spread is defined as the farthest point along the wall in the x-direction above the MREs that the droplet reaches after impact. The results of the maximum spread are shown in Figure 4.17 and Figure 4.18. The farthest point the droplet reaches is above a cavity between the MREs, and this is the point where the spread is measured. The spread and rebound behavior of the droplet, shown in a sequence of images in Figure 4.19, demonstrates that the droplet spreads out across the top of the MREs, breaks apart into smaller droplets, and remnants of the droplet rebound off the surface while satellite droplets remain scattered along the surface. The maximum spreads for the axisymmetric 100 CPR and 200 CPR meshes are very similar, as is the qualitative appearance of the simulations indicating that the mesh resolution is adequate.

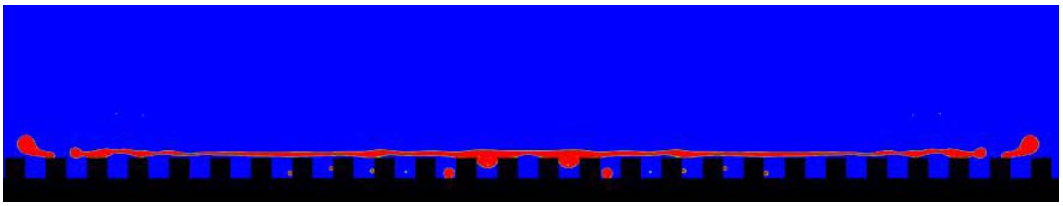

222.968 μm

Figure 4.17 Qualitative results for InterFoam on axisymmetric domain with 100 CPR for 50 μm-diameter droplet impacting dry surface with MREs at 53.6 *m/s*. Size of MREs on surface is 5 μm x 5 μm.

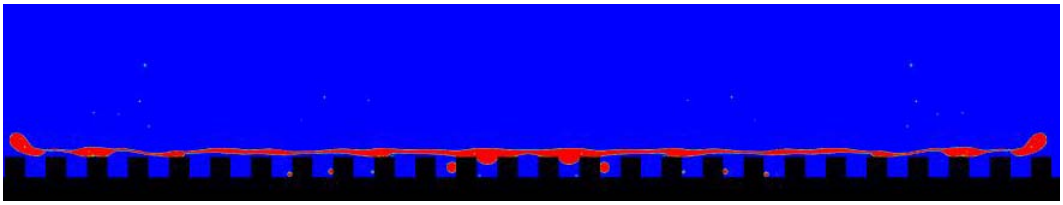

252.79 μm

Figure 4.18 Qualitative results for InterFoam on axisymmetric domain with 200 CPR for 50 μm-diameter droplet impacting dry surface with MREs at 53.6 *m/s*. Size of MREs on surface is 5 μm x 5 μm.

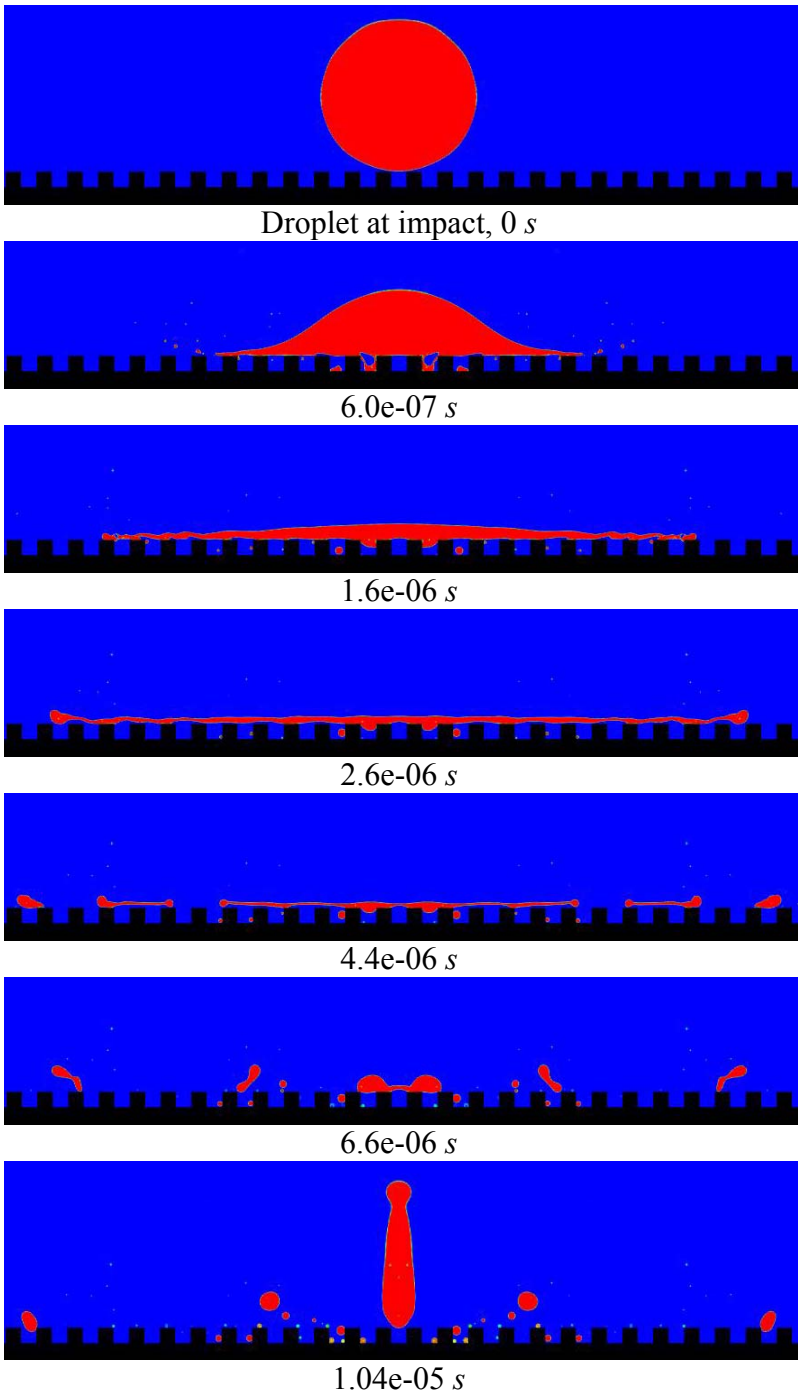

Figure 4.19 Sequence of qualitative results on axisymmetric domain with 200 CPR. Times listed are approximate and are referenced to an estimated time of impact.

4.2.3.2 MREs with Saturated Surface

The cavities between the structured MREs were filled with water to understand their performance degradation in the presence of a thin film, which corresponds to a saturated surface under conditions of high humidity. The size of the MREs and domains are identical to those used in the dry impact studies in Section 4.2.3.1. The maximum spread is defined in the same manner as for the dry MRE. Again, maximum spread values for the 100 and 200 CPR domains were nearly identical verifying that the mesh resolution is adequate. It is observed in Figure 4.20 and Figure 4.21 that the water filling the cavities between the MREs combines with the impacting droplet as it spreads over the surface. This creates a pocket of air in the cavity and the contact angle becomes active. As these "bubbles" grow, the air pocket begins to affect the behavior. This is due to the simulation domain being an axisymmetric wedge and the "bubble" being trapped, unable to escape. The water contained in the cavities bulging above the MREs is due to surface tension. Note that the maximum spread in Figure 4.21 is similar to the maximum spread shown for the smooth dry surface in Figure 4.13, which is somewhat smaller in extent than the spread for the dry surface with the MRE shown in Figure 4.18. The droplet spread can be visualized in the time sequence shown in Figure 4.22. No droplet rebound was observed with this case due to the large bubbles that developed under the droplet at the surface. These results demonstrate that the effectiveness of the MRE is degraded due to the presence of the film layer, i.e., high humidity. However, questions remain about the accuracy of the simulation. It is hypothesized that three-dimensional simulations are necessary to resolve this issue and accurately predict the rebound behavior.

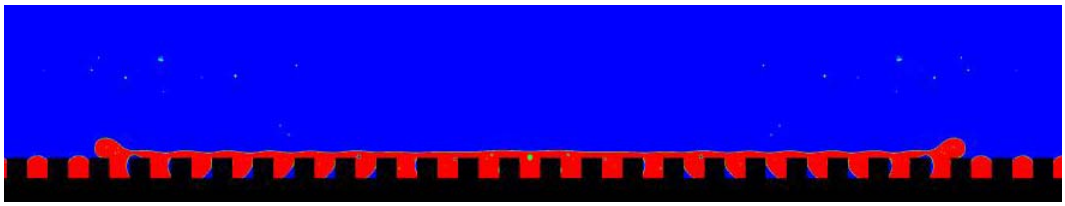

208.948 μm

Figure 4.20 Qualitative results for InterFoam on axisymmetric domain with 100 CPR for 50 μm-diameter droplet impacting wetted surface with MREs at 53.6 *m/s*. Size of MREs on surface is 5 μm x 5 μm. Depth of water on surface is 5 μm.

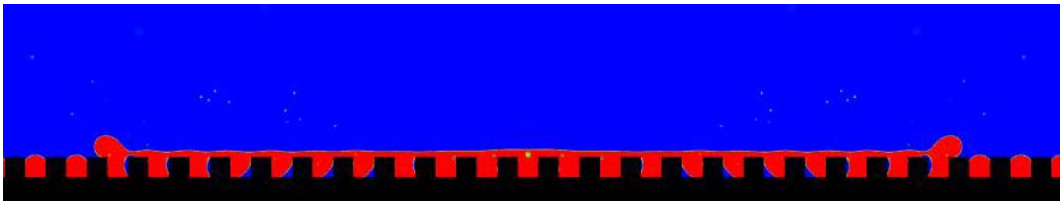

209.488 μm

Figure 4.21 Qualitative results for InterFoam on axisymmetric domain with 200 CPR for 50 μm-diameter droplet impacting wetted surface with MREs at 53.6 *m/s*. Size of MREs on surface is 5 μm x 5 μm. Depth of water on surface is 5 μm.

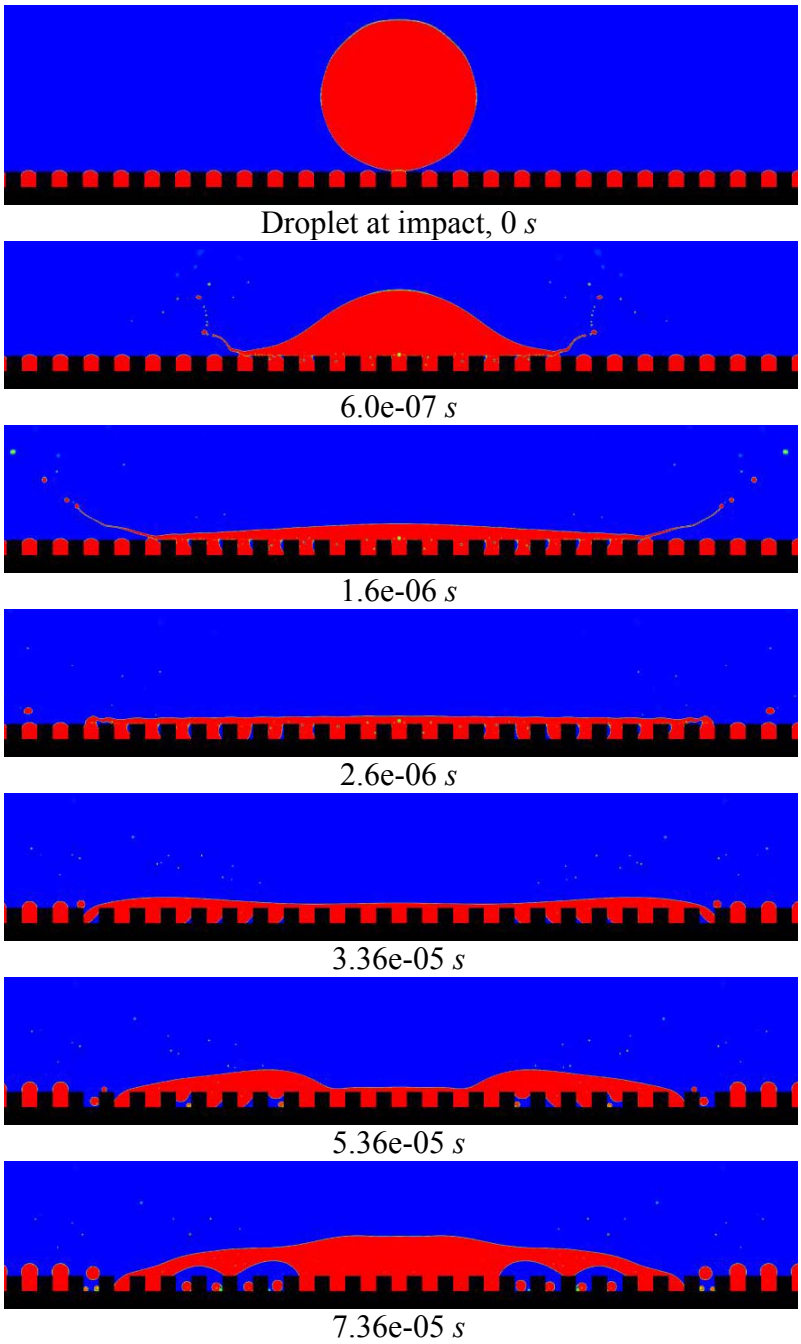

Figure 4.22 Sequence of qualitative results for InterFoam on axisymmetric domain with 200 CPR. Times listed are approximate and are referenced to an estimated time of impact.

CHAPTER V

CONCLUSIONS

The numerical simulation of single droplets impacting a surface is complicated with several influential variables such as surface and fluid properties. Complex physics and contrasting length scales present challenges for simulations.

The validation of InterFoam, an open-source VOF solver, for droplets on a dry hydrophobic demonstrated the capabilities of OpenFOAM®. The results of the validation showed that for very viscous droplets, i.e., the glycerin droplet in Case I, InterFoam accurately captures the behavior of the droplet after impact. Simulations for a water droplet impacting a hydrophobic surface demonstrated the validity of the use of axisymmetric domains and a refinement study was performed. It was observed that using the 40 CPR domain demonstrated the best agreement with experimental results in terms of maximum droplet spread. Although the solution could not be called mesh converged, it did show a clear trend as the mesh was refined. The case in which a specified velocity was given to the droplet resulted in an over-prediction of the maximum spread. This is likely due to the influence of the air below the droplet as it falls. Though images in a video obtained during the experiment indicated that the droplet shape near impact is elliptical rather than spherical, the numerical simulations for an elliptical droplet consistently demonstrated an over-prediction of spread after impact. It is hypothesized that three-dimensional simulations would be able to resolve issues such as air bubbles

trapped at the surface that can cause inaccurate results in axisymmetric simulations and are recommended for high speed droplet impacts when splashing is involved.

The primary finding of this research was the effect of structured MREs for aircraft icing applications under dry conditions and high humidity conditions, i.e., when visible moisture is present. Simulations were performed on axisymmetric domains to establish mesh spacing and identify trends. Droplet impacts on a smooth dry surface on an axisymmetric domain produced acceptable results; however, issues arose with the droplets impacting a smooth surface with a liquid film and surfaces with MREs, both dry and with a film. Though the splashing mechanism was accurately demonstrated on the axisymmetric domain, a three-dimensional simulation is recommended to accurately capture the phases of the evolution of splashing due to the physical complexity of splashing at high speed impact. Pockets of air can become trapped at the surface with no way for it to escape in an axisymmetric domain. Axisymmetric domains are not ideal for impacts on surfaces with MREs because they represent a wedge-shaped domain on which the MREs are concentric circles instead of parallel ridges. Thus, three-dimensional simulations should be used to evaluate the effectiveness of structured MREs on the surface. Information from the axisymmetric simulations for the spread and rebound of the droplet after impacting can be used as a starting point.

REFERENCES

[1] Abbott, I. H., & von Doenhoff, A. E. (1959). *Theory of Wing Sections: Including a Summary of Airfoil Data.* Dover Publications.

[2] Autumn, K., Liang, Y. A., Hsieh, S. T., Zesch, W., Chan, W. P., Kenny, T. W., et al. (2000). Adhesive Force of a Single Gecko Foot-Hair. *Nature , 405* , 681-685.

[3] Barthlott, W., & Neinhuis, C. (1997). Purity of the sacred lotus, or escape from contamination in biological surfaces. *Planta , 201* (1), 1-8.

[4] Behrens, T. (2009). OpenFOAM's basic solvers for linear systems of equations: solvers, preconditioners, smoothers. Notes from *CFD with OpenSource Software* course, Chalmers University of Technology.

[5] Berberovic, E., van Hinsberg, N., Jakirlic, S., Roisman, I., & Tropea, C. (2009). Droplet Impact onto a Liquid Layer of Finite Thickness: Dynamics of the Cavity Evolution. *Physical Review E , 79* (3), 036306-1-036306-15.

[6] Bertin, J. J., & Cummings, R. M. (2008). *Aerodynamics for Engineers* (5th ed.). Pearson/Prentice Hall.

[7] Brackbill, J., Kothe, D., & Zemach, C. (1992). A Continuum Method for Modeling Surface Tension. *Journal of Computational Physics , 100* (2), 335-354.

[8] Breau d'Enquetes et d'Analyses (BEA). *Interim report on the accident on 1st June 2009 to the Airbus A330-203, registered F-GZCP, operated by Air France, Flight AF 447 Rio de Janeiro.* Paris.

[9] Burden, R. L., & Faires, J. D. (2004). *Numerical Analysis* (8th ed.). Belmont: Brooks Cole.

[10] Burtnett, E., Thompson, D., Jung, S., & Raps, D. (2012). A Comparison of VOF Simulations with Experimental Data for Droplet Impact on a Dry Surface. *AIAA Aerospace Sciences Meeting*, (pp. AIAA-2012-0092). Nashville.

[11] Cao, L., Jones, A., Sikka, V., Wu, J., & Gao, D. (2009). Anti-Icing Superhydrophobic Coatings. *Langmuir , 25* (21), 12444-12448.

[12] Cerne, G., Petelin, S., & Tiselj, I. (2001). Coupling of the Interface Tracking and the Two-Fluid Models for the Simulation of Incompressible Two-Phase Flow. *Journal of Computational Physics , 171* (2), 776-804.

[13] Clift, R., & Gauvin, W. H. (1970). The motion of particles in turbulent gas streams. *Proc. Chemeca E.C.A. , 1*, 14-24.

[14] Cossali, G. E., Coghe, A., & Marengo, M. (1997). The impact of a single drop on a wetted solid surface. *Experiments in Fluids , 22* (6), 463.

[15] Crowe, C. (2006). *Multiphase Flow Handbook.* Boca Raton: CRC Press.

[16] Davis, A., Yeong, Y., Steele, A., Loth, E., & Bayer, I. (2012). Spray Impact Resistance of Superhydrophobic Nanocomposite Coating. *AIAA Aerospace Sciences Meeting*, (pp. AIAA-2012-0091). Nashville.

[17] de Gennes, P. (1985). Wetting: Statics and Dynamics. *Review of Modern Physics , 57* (3), pp. 827-863.

[18] Fluent 12.0. (2009). Users Guide. *ANSYS, Inc.* Lebanon, NH.

[19] Fukai, J., Shiiba, Y., Yamamoto, T., Miyatake, O., Poulikakos, D., Megaridis, C., et al. (1995). Wetting Effects on the Spreading of a Liquid Droplet Colliding with a Flat Surface: Experiment and Modeling. *Physics of Fluids , 7* (2), 236-247.

[20] Fukai, J., Zhao, Z., Poulikakos, D., Megaridis, C., & Miyatake, O. (1993). Modeling of the Deformation of a Liquid Droplet Impinging upon a Flat Surface. *Physics of Fluids A , 5* (11), 2588-2599.

[21] Gao, X. F., & Jiang, L. (2004). Water-Repellent Legs of Water Striders. *Nature , 432* , 36.

[22] Gao, X. F., Yan, X., Yao, X., Xu, L., Zhang, K., Zhang, J. H., et al. (2007). The Dry-Style Antifogging Properties of Mosquito Compound Eyes and Artificial Analogues Prepared by Soft Lithography. *Adv. Mater. , 19* , 2213-2217.

[23] Grunau, D., Chen, S., & Eggert, K. (1993). A lattice-Boltzmann model for multiphase flows. *Physics of Fluids , A5*, 2557-2562.

[24] Gunjal, P., Ranade, V., & Chaudhari, R. (2005). Dynamics of Drop Impact on Solid Surface: Experiments and VOF Simulations. *AIChE Journal , 51* (1), 59-79.

[25] Gunstensen, A., Rothman, D., Zaleski, S., & Zanetti, G. (1991). Lattice-Boltzmann model of immiscible fluids. *Physical Review A , 43*, 4320-4327.

[26] Guo, Z., Weimin, L., & Bao-Lian, S. (2011). Featured Article: Superhydrohobic surfaces: From natural to biomimetic to functional. *Journal of Colloid and Interface Science , 353*, 335-355.

[27] Hansen, F. K. (nd). The Measurement of surface energy of polymer by means of contact angles of liquids on solid surfaces: A short overview of frequently used methods. *Department of Chemistry University of Oslo*.

[28] Hill, E., Roy, M., Botura, G., Riley, J., Dumunt, C., Pullin, D., et al. (2006). Invesitgations of Performance of Pneumatic Deicing Boots, Surface Ice Dectectors, and Scaling of Intercycle Ice. *DOT/FAA AR-06/48* .

[29] Hirt, C., & Nichols, B. (1981). Volume of Fluid (VOF) Method for the Dynamics of Free Boundaries. *Journal of Computational Physics , 39* (1), 201-225.

[30] Issa, R. (1986). Solution of the Implicitly Discretised Fluid Flow Equations by Operator-Splitting. *Journal of Computational Physics , 62* (1), 40-65.

[31] Jung, S., Dorrestijn, M., Raps, D., Das, A., Megaridis, C., & Poulikakos, D. (2011). Are Superhydrophobic Surfaces Best for Icephobicity? *Langmuir , 27 (6)* , 3059-3066.

[32] Kuo-Long, P., & Chun-Yu, H. (2010). Droplet impact upon a wet surface with a varied fluid and surface properties. *Journal of Colloid and Interface Science , 35* (2), 186-193.

[33] Lunkad, S. F., Buwa, V. V., & Nigam, K. P. (2007). Numerical Simulations of Drop Impact and Spreading on Horizontal and Inclined Surfaces. *Chemical Engineering Science , 62* (24), 7214-7224.

[34] Mishchenko, L., Hatton, B., Bahadur, V., Taylor, A., Krupenkin, T., & Aizenberg, J. (2010). Design of Ice-Free Nanostructured Surfaces Based on Repulsion of Impacting Water Droplets. *ACS Nano , 4* (12), 7699-7707.

[35] Mundo, Chr., Sommerfeld, M., Tropea, C. (1995). Droplet-wall collisions: Experimental studies of the deformation and breakup process. *International Journal of Multiphase Flow, 21*, 151-173.

[36] Nourgaliev, R., Dinh, T., Theofanous, T., & Joseph, D. (2003). The lattice Boltzmann equation method: theoretical interpretation, numerics and implications. *International Journal of Multiphase Flow , 29*, 117-169.

[37] *OpenCFD Ltd.* (n.d.). Retrieved from http://www.opencfd.co.uk

[38] *OpenFOAM documentation, User Guide*. (n.d.). Retrieved from http://www.openfoam.com/docts/user

[39] Osher, S., & Sethian, L. (1988). Fronts propagating with curvature-depending speed: algorithms based on Hamilton-Jacobi formulation. *Journal of Computational Physics , 79*, 12-49.

[40] Patankar, N. Mimicking the lotus effect: Influence of double roughness structures and slender pillars. *Langmuir , 20* (19), 8209-8213.

[41] Raps, D. (2011, April 18). "MSU Update," Email to Thompson, D., and Burtnett, E.

[42] Raps, D. (2011, June 1). "Questions about droplet data," Email to Thompson, D., and Burtnett, E.

[43] Rieber, M., & Arnold, F. (1999). A numerical study on the mechanism of splashing. *International Journal of Heat and Fluid Flow , 20*, 455-461.

[44] Rioboo, R. R., Marengo, M. M., Cossali, G. E., & Tropea, C. C. (2000). Comparison of Drop Impact: Dry and Wetted Cases. *Ilass Europe , II* (11).

[45] Rioboo, R., Bauthier, C., Conti, J., Voue, M., & De Coninck, J. (2003). Experimental invesitgation of splash and crown formation during single drop impact on wetted surfaces. *Experiments in Fluids , 35* (6), 648.

[46] Rioboo, R., Marengo, M., & Tropea, C. (2001). Outcomes of a Drop Impact on Solid Surface. *Atomization and Sprays , 11* (2), 155-65.

[47] Rioboo, R., Marengo, M., & Tropea, C. (2002). Time Evolution of Liquid Drop Impact on Solid, Dry Surface. *Experiments in Fluids , 33* (1), 112-124.

[48] Roisman, I., Opfer, L., Tropea, C., Raessi, M., Mostaghimi, J., & Chandra, S. (2008). Drop Impact onto a Dry Surface: Role of the Dynamic Contact Angle. *Colloids and Surface A Physiochemical and Engineering Aspects , 322* (1-3), 193-191.

[49] Rusche, H. (2002). Computational Fluid Dynamics of Dispersed Two-Phase Flows at High Phase Fractions. London, UK: Imperial College of Science, Technology, and Medicine.

[50] Shan, X., & Chen, H. (1993). Lattice Boltzmann model for simulating flows with multiple phases and components. *Physics Review E , 47*, 1815-1819.

[51] Shu, B., Dammel, F., & Stephan, P. (2007). Implementation of the Level Set Method into OpenFOAM for Capturing the Free Interface in Incompressible Fluid Flows. *OpenFOAM International Conference* . Old Windsor, UK.

[52] Sikalo, S., Tropea, C., & Ganic, E. N. (2005). Dynamic Wetting Angle of a Spreading Droplet. *Experimental Thermal and Fluid Science , 29* (7), 795-802.

[53] Sussman, M., Smereka, P., & Osher, S. (1994). A Level Set Approach for Computing Solutions to Incompressible Two-Phase Flow. *Journal of Computational Physics , 114*, 146-159.

[54] U.S. Department of Transportation, F. A. (1993, April 9). Federal Aviation Regulations Part 23, Subpart F, Safety Equipment, Ice Protection, 58 FR 18977.

[55] U.S. Department of Transportation, N. T. (1996). In-Flight Icing Encounter and Loss of Control America Eagle Flight 4184, Avions de Transport Regional (ATR) Model 72-212, Roselawn, Indiana October 31, 1994, Volume 1 Safety Board Report. *NTSB/AAR-96/01* .

[56] U.S. Department of Transportation, N. T. (1999). In-Flight Icing Encounter and Uncontrolled Collision with Terrain Comair Flight 3272 Embraer EMB-120RT, N265CA Monroe, Michigan January 9, 1997. *NTSB/AAR-98/04* .

[57] Unverdi, S. O., & Tryggvason, G. (1992). A front tracking method for viscous incompressible, multi-fluid flows. *Journal of Computational Physics , 100*, 25-37.

[58] Wang, A., & Chen, C. Splashing impact of a single drop onto very thin liquid films. *Physics of Fluids , 12* (9), 2155-2158.

[59] Xiao, J., Mackie, K., Osborne, J., Seebergh, J., & Chaudhuri, S. (2011). In-Silico Environment for Designing Anti-Ice Surfaces. *SAE 2011 International Conference on Aircraft and Engine Icing and Ground Deicing.* Chicago.

[60] Yarin, A. (2006). Droplet Impact Dynamics: Splashing, Spreading, Recedzing, Bounding... *Annual Review of Fluid Mechanics , 38*, 159-92.

[61] Zheng, Y. M., Gao, X. F., & Jiang, L. (2007). Directional Adhesion of Superhydrophobic Butterfly Wings. *Soft Matter , 3*, 178-182.